MATERIALS SCIENCE

Confining metal-halide perovskites in nanoporous thin films

Stepan Demchyshyn,[1,2,3]* Janina Melanie Roemer,[4]* Heiko Groiß,[5,6] Herwig Heilbrunner,[1] Christoph Ulbricht,[1†] Dogukan Apaydin,[1] Anton Böhm,[4] Uta Rütt,[7] Florian Bertram,[7] Günter Hesser,[6] Markus Clark Scharber,[1] Niyazi Serdar Sariciftci,[1] Bert Nickel,[4,8] Siegfried Bauer,[2] Eric Daniel Głowacki,[9‡] Martin Kaltenbrunner[2,3‡]

Controlling the size and shape of semiconducting nanocrystals advances nanoelectronics and photonics. Quantum-confined, inexpensive, solution-derived metal halide perovskites offer narrowband, color-pure emitters as integral parts of next-generation displays and optoelectronic devices. We use nanoporous silicon and alumina thin films as templates for the growth of perovskite nanocrystallites directly within device-relevant architectures without the use of colloidal stabilization. We find significantly blue-shifted photoluminescence emission by reducing the pore size; normally infrared-emitting materials become visibly red, and green-emitting materials become cyan and blue. Confining perovskite nanocrystals within porous oxide thin films drastically increases photoluminescence stability because the templates auspiciously serve as encapsulation. We quantify the template-induced size of the perovskite crystals in nanoporous silicon with microfocus high-energy x-ray depth profiling in transmission geometry, verifying the growth of perovskite nanocrystals throughout the entire thickness of the nanoporous films. Low-voltage electroluminescent diodes with narrow, blue-shifted emission fabricated from nanocrystalline perovskites grown in embedded nanoporous alumina thin films substantiate our general concept for next-generation photonic devices.

INTRODUCTION

Tuning the bandgap of semiconductors via quantum size effects launched a technological revolution in optoelectronics, advancing solar cells (*1*, *2*), quantum dot light-emitting displays (*3*), and solid state lasers (*4*). Next-generation devices seek to use low-cost, easily processable semiconductors. A promising class of such materials is metal-halide perovskites (*5*), which currently propels research on emerging photovoltaics (*6*–*8*). Their narrowband emission permits very high color purity in light-emitting devices and vivid lifelike displays paired with low-temperature processing through printing-compatible methods (*9*–*13*). The success of perovskites in light-emitting devices is conditional upon finding reliable strategies to tune the bandgap while preserving good electrical transport. Thus far, color can be tuned chemically by mixed halide stoichiometry and by synthesis of colloidal nanoparticles (*14*, *15*). Here, we introduce a general strategy of confining perovskite nanocrystallites (less than 10 nm) directly within device-relevant solid-state thin-film formats without the use of colloidal stabilization. With nanoporous alumina (npAAO) or nanoporous silicon (npSi) scaffolds serving as templates for the growth of perovskite nanocrystallites on transparent conductive oxides or silicon wafers, we achieve fine-tuning of the bandgap across a wide color gamut from near-infrared (NIR) to ultraviolet (UV). Confinement in npSi facilitates a ~50-nm hypsochromic shift from green to blue photoluminescence (PL) for cesium-bromide perovskite nanocrystals. By infiltrating npAAO templates on transparent conductive substrates, we fabricate perovskite light-emitting diodes (LEDs) that achieve blue-shifted narrowband [full width at half maximum (FWHM), 17 nm] emission. Our demonstrations corroborate bandgap engineering through confinement in nanoporous solids as a powerful tool to precisely control the emission wavelength of perovskite nanocrystals in next-generation, solution-derived photonic sources.

Quantum confinement was recognized as an auspicious feature in two-dimensional (2D) layered organic-inorganic hybrid perovskites in the pioneering work of Mitzi *et al.* (*5*, *16*, *17*) in the 1990s. Renewed interest in the alkylammonium lead halide ($APbX_3$) perovskites inspired elaboration of colloidal chemistry techniques, such as utilizing nanocrystalline capping (*18*, *19*), two-step processes with PbI_2 nanocrystals as templates (*20*), emulsion synthesis (*21*), and reprecipitation (*22*–*24*), to achieve crystals featuring quantum size effects (*25*, *26*). Colloidal nanocrystals based on the all-inorganic $CsPbX_3$ system were developed by Protesescu *et al.* (*15*), which exhibit bandgap tunability via halide composition (*14*) and quantum size effects (*15*). The size dependency of the observed hypsochromic shifts can be well approximated by the confinement energy in a spherical potential well for crystallite sizes above 6 nm (*15*). In a ligand-free approach, nanoporous silica powder can be used as a template to achieve monodisperse lead halide perovskite crystals with quantum confinement (*27*, *28*). Here, the insulating nature of the silica precluded potential electronic device applications. Templating approaches based on mesoporous alumina to achieve nanoparticles (*29*, *30*) were reported in geometries not allowing for electrical excitation.

[1]Linz Institute for Organic Solar Cells (LIOS), Institute of Physical Chemistry, Johannes Kepler University Linz, Altenbergerstraße 69, 4040 Linz, Austria. [2]Department of Soft Matter Physics, Johannes Kepler University Linz, Altenbergerstraße 69, 4040 Linz, Austria. [3]Linz Institute of Technology (LIT), Altenbergerstraße 69, 4040 Linz, Austria. [4]Faculty of Physics and Center for NanoScience (CeNS), Ludwig-Maximilians-University München, Geschwister-Scholl-Platz 1, 80539 Munich, Germany. [5]Christian Doppler Laboratory for Microscopic and Spectroscopic Material Characterization, Johannes Kepler University Linz, Altenbergerstraße 69, 4040 Linz, Austria. [6]Center for Surface and Nanoanalytics, Johannes Kepler University Linz, Altenbergerstraße 69, 4040 Linz, Austria. [7]Deutsches Elektronen-Synchrotron (DESY) Photon Science, Notkestraße 85, 22603 Hamburg, Germany. [8]Nanosystems Initiative Munich, Schellingstraße 4, 80799 München, Germany. [9]Laboratory of Organic Electronics, Department of Science and Technology, Campus Norrköping, Linköpings Universitet, Bredgatan 33, SE-601 74 Norrköping, Sweden.
*These authors contributed equally to this work.
†Present address: Institute for Polymeric Materials and Testing (IPMT), Johannes Kepler University Linz, Altenbergerstraße 69, 4040 Linz, Austria.
‡Corresponding author. Email: eric.glowacki@liu.se (E.D.G.); martin.kaltenbrunner@jku.at (M.K.)

RESULTS

Nanoscale reactors concept

Here, we introduce solid-state nanoscale templating in a thin-film format to confine the growth of the perovskite directly within device-relevant architectures (Fig. 1A). This method yields perovskite nanocrystals with sizes of a few nanometers. We characterize nanocrystalline methylammonium lead trihalide (ncMAPbX_3), with chloride, bromide, and iodide (X = Cl, Br, I) perovskites, as well as nanocrystalline cesium lead tribromide (ncCsPbBr_3). We demonstrate the concept on two different nanoscaffold films, each with specific advantages. The first template comprises anodic aluminum oxide nanotubes (npAAO) with diameters of ~6 to 8 nm and lengths from 20 up to hundreds of nanometers. The second template is composed of an electrochemically etched npSi layer tens of micrometers thick renowned for its 3D spongy network of nanopores with tunable sizes ranging from 2 to 10 nm (*31*, *32*). Both nanoscale solid-state scaffolds are prepared using scalable, room temperature anodization (detailed in Materials and Methods). The infiltrated pores serve as nanoreactors, constraining the growth of the perovskite crystals that form from the solution-borne precursors. We imaged ~150-nm-thick npAAO cross sections using scanning transmission electron microscopy (STEM) (Fig. 1B). The projection of the STEM image resolves both a network of perovskite nanocrystals partially filling the nanopores and the surrounding AAO matrix. Here, the nucleation density (resulting in the apparent nucleation profile) is controllable via the concentration of the precursor solution (see the Supplementary Materials). Exfoliated flakes of an npSi sponge filled with nanocrystals are shown in Fig. 1C. The perovskite nanocrystals appear dark (due to diffraction and mass contrast) in both matrices in these bright-field STEM (BF-STEM) images. We find blue-shifted PL in all cases; nanocrystalline methylammonium lead triiodide (ncMAPbI_3) grown in npAAO blue-shifts by 62 nm, whereas ncMAPbBr_3 and ncCsPbBr_3 shift by 14 and 16 nm, respectively (Fig. 1D). Blue shifts in the PL are common in organic conjugated molecules when isolated (*33*, *34*), for example, in solution or in npAAO (*35*–*37*) and silica (*38*, *39*). In contrast, solid-state nanopore templating of nanocrystalline perovskites at sizes less than the exciton radius in the semiconductor (*40*) gives rise to strong quantum and dielectric confinement effects responsible for the observed blue-shifted emission. The npSi, featuring smaller pores than npAAO, affords shifts of up to 151 nm for ncMAPbI_3 and ca. 50 nm for ncMAPbBr_3 and ncCsPbBr_3, and typically 15 nm for ncMAPbCl_3 (Fig. 1E). These shifts correspond to significant bandgap changes of the perovskites of up to 0.37 eV for MAPbI_3, 0.25 eV for MAPbBr_3 and CsPbBr_3, and 0.11 eV for the already large bandgap MAPbCl_3. The magnitude of these shifts depends on the material, in line with the trend of the respective bandgap energies and the associated reduced exciton masses (*15*, *41*). Our methods are not limited to single-halide precursors. Color tuning via a combination of size effects and adjusting halide compositional stoichiometry is possible in both npSi and npAAO (fig. S1), eventually allowing accessing the whole visible spectral range. The uniform blue-shifted emission of nanocrystalline perovskites in npAAO under UV illumination demonstrates that the whole sample area emits homogeneously over square centimeters (Fig. 1F). The blue shifts are even more pronounced for the npSi matrix; here, we achieve red emission (640 nm) from the NIR-emitting bulk MAPbI_3 and blue color (480 nm) from the normally green bulk CsPbBr_3 (Fig. 1G).

Color tunability

Precise nanopore-size tunability is a compelling advantage of the npSi system. We use a galvanostatic method (*42*) that allows pore size tuning by changing the anodization current density (detailed in Materials and Methods). The as-prepared porous silicon samples are hydride-terminated and weakly photoluminescent. We observed that a radio-frequency oxygen plasma treatment completely eliminates the PL of the porous silicon samples (fig. S2). This procedure accomplishes the dual role of extinguishing native luminescence and creating a surface that is highly wettable by the perovskite precursor solution. We find that the PL of MAPbI_3 becomes increasingly blue-shifted as the pore size is reduced, from an initial bulk-like NIR emission at 791 nm across the visible red range, with a maximal hypsochromic shift to 640 nm (Fig. 2A). MAPbBr_3 (Fig. 2B) and CsPbBr_3 (Fig. 2C) behave similarly; here, the normally green-emitting materials can be shifted to give visibly cyan (485 nm) and blue (479 nm) emission. In all these cases, the peak emission wavelength varies linearly with the anodization current used to prepare the pores (fig. S3), indicating a dependence of the bandgap on nanopore size. Even the emission of the wide-bandgap MAPbCl_3 can be shifted further into the UV range, well below 400 nm (Fig. 2D). Hypsochromic shifts obtained with transparent, thin-film npAAO templates on glass slides (250-nm npAAO; see Materials and Methods) are also shown (Fig. 2, A to C). The observed shifts qualitatively agree well with reported blue shifts for different methods of obtaining nanocrystals or nanoplatelets (*20*, *28*). We find a PL quantum yield (PLQY) of up to 25% ($\bar{x}$ = 13.76%, σ = 9.17%, n = 4) for ncMAPbI_3, up to 60% ($\bar{x}$ = 36.04%, σ = 16.23%, n = 4) for ncMAPbBr_3, and up to 90% ($\bar{x}$ = 54.84%, σ = 31.98%, n = 4) for ncCsPbBr_3 in npAAO (see Materials and Methods for details). The PLQY of our nanoparticle emitters is significantly higher than what we observe for the bulk semiconductor films (<1 to 2%) and fits well within the range reported for other nanosized perovskite materials (*27*, *28*, *30*, *43*). Time-resolved PL measurements (fig. S4) show a short lifetime for our nanocrystals (0.3 to 3 ns), whereas bulk films are longer-lived (3 to 25 ns). This behavior is known for quantum dot systems (*15*, *44*) and also observed for MAPbI_3 films with varying crystallite dimensions (*45*) and for MAPbBr_3 in mesoporous silica (*27*).

Here, we show that the confinement effects enable broad tunability windows in emission color from single-halide precursors, leaving the spectral regions from 640 to 530 nm and from 479 to 405 nm unaddressed. To illustrate the generality of our approach, we complete these gaps by complementing the confinement effects with mixed halide stoichiometry. We demonstrate this with mixed iodide-bromide nanocrystals in npAAO, resulting in yellow emission, and with mixed bromide-chloride perovskites in npSi, resulting in deeper blue emission (fig. S1). Besides determining crystallite size, our thin-film oxide templates enhance the stability and largely prevent degradation of the nanocrystals when excited with blue light (405 nm) under ambient conditions. Whereas bulk films decay rather rapidly under these conditions, the PL intensity of ncMAPbBr_3 in 250-nm-thick npAAO (Fig. 2E) initially increases by roughly 40% and then stabilizes without further changes in shape of the PL signal (Fig. 2F). Similar results are obtained when comparing CsPbBr_3 with ncCsPbBr_3 (Fig. 2, G and H), wherein an initial increase is followed by a delayed decay back to the original values. We believe that the alumina matrix serves as an encapsulation that largely prevents ingress of oxygen and water. The initial increase in PL intensity may be attributed to light curing with oxygen, reducing nonradiative charge recombination by deactivating the respective trapping sites (*46*). Encapsulating ncMAPbBr_3 and ncCsPbBr_3 samples with epoxy and glass slides further corroborates these findings because the PL intensity remains essentially unchanged in the absence of oxygen and water. This in turn demonstrates the stability

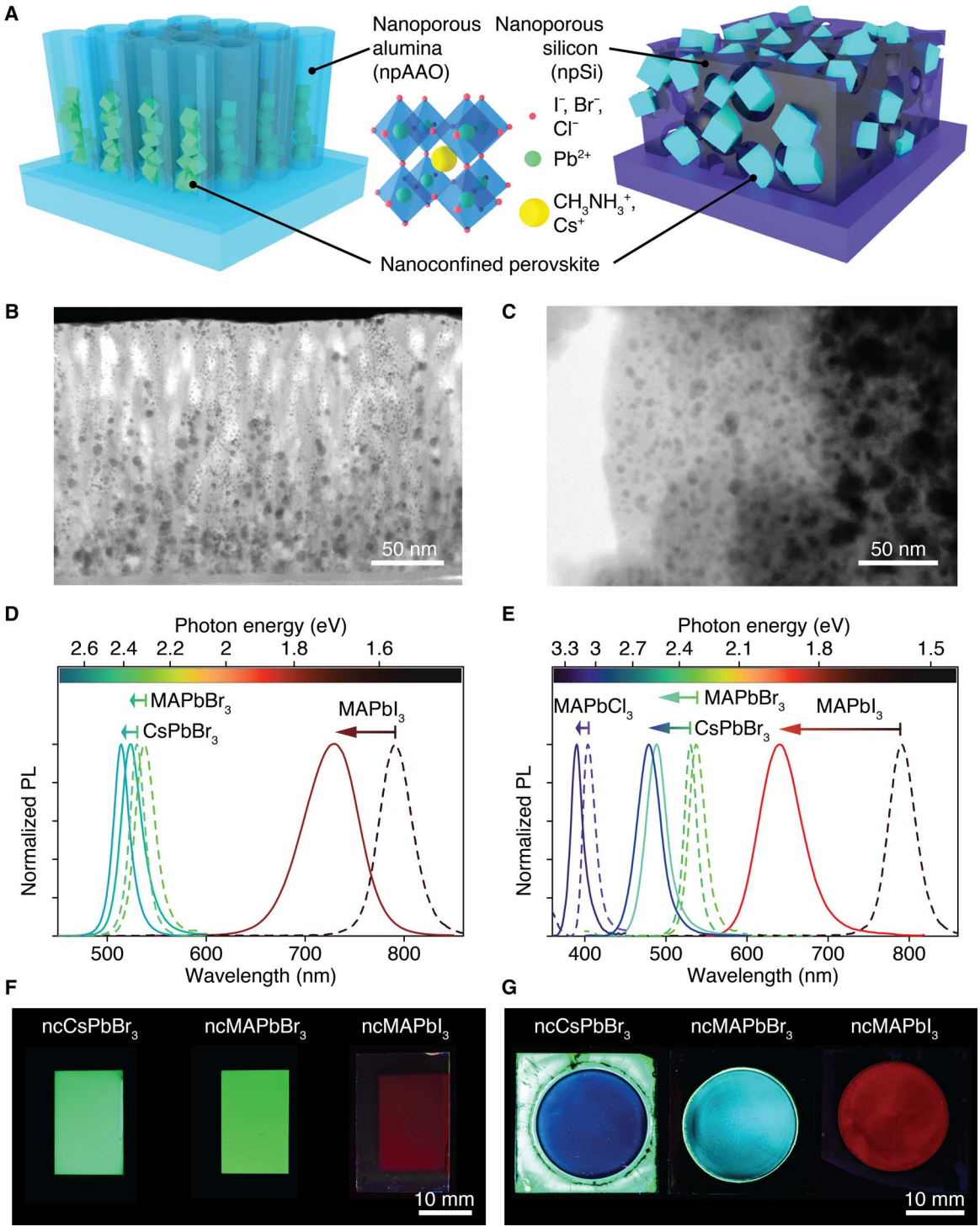

Fig. 1. Metal-halide perovskites confined in nanoporous films. (**A**) Schematic of nanoscale solid film templates (npAAO on the left and npSi on the right) infused with perovskite nanocrystals. The chemical structure of methylammonium lead trihalide (ncMAPbX_3) and cesium lead trihalide perovskites (ncCsPbX_3), with chloride, bromide, and iodide (X = Cl, Br, I), is shown in the middle. (**B**) BF-STEM image of a 170-nm-high, ~100-nm-thick npAAO filament, indicating alumina nanopores of 6 to 8 nm in diameter, partially filled with conjoined perovskite nanocrystals. (**C**) Exfoliated flake of npSi filled with $MAPbI_3$, imaged by BF-STEM. Perovskite nanocrystals appear dark because of their diffraction and mass contrast. Nanocrystals on the right appear aggregated; this is an imaging artefact caused by an increase in flake thickness. (**D**) PL of ncMAPbI_3 grown in npAAO (solid red line), blue-shifted by 62 nm. ncMAPbBr_3 (solid green line) and ncCsPbBr_3 (solid cyan line) are shifted by 14 and 16 nm, respectively. Dashed lines show bulk film PL. (**E**) PL of perovskite-infiltrated npSi. These smaller pores result in a 150-nm shift for ncMAPbI_3 (solid red line), 52 nm for ncMAPbBr_3 (solid cyan line), 51 nm for ncCsPbBr_3 (solid blue line), and 14 nm for ncMAPbCl_3 (solid purple line). Dashed lines indicate bulk film PL. (**F** and **G**) Photographs of square centimeter–scaled thin films of nanocrystalline perovskites under UV illumination: npAAO on glass slides (F) and npSi on Si wafers (G). The circular areas in (G) are nanoporous.

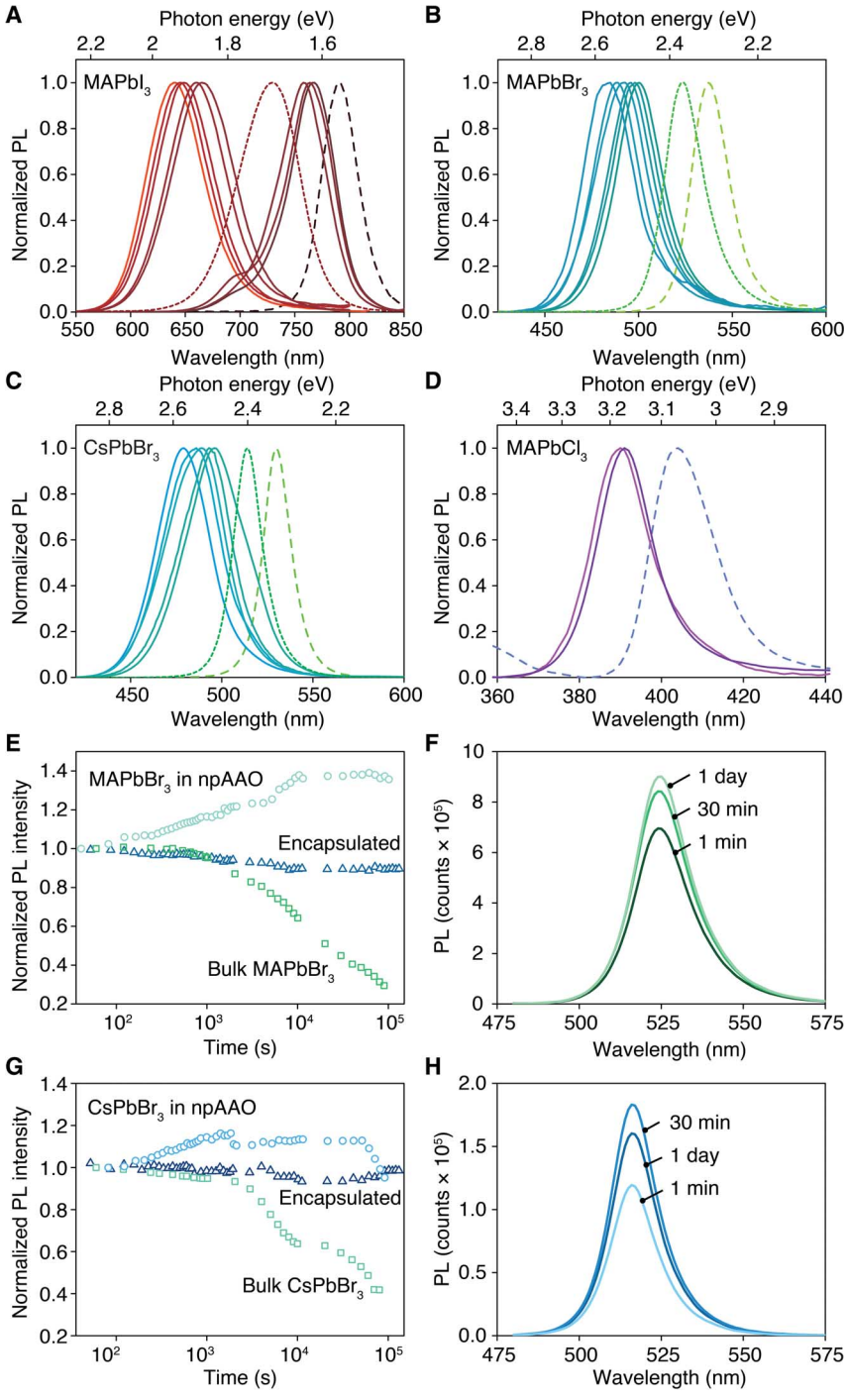

Fig. 2. PL tuning and stability of perovskites confined in nanoporous films. The dashed lines represent the bulk PL, whereas the dotted lines are the PL of perovskites in npAAO. Solid lines correspond to the PL of perovskites grown in npSi, with successive blue-shifted peaks originating from samples with progressively smaller pore sizes. (**A**) $MAPbI_3$ bulk versus crystals confined in npAAO and in eight differently sized npSi scaffolds. A clear transition from NIR emission to visible red is observed. (**B**) $MAPbBr_3$ bulk versus crystals confined in npAAO and six differently sized npSi scaffolds, showing emission shifting from green to blue. (**C**) $CsPbBr_3$ bulk versus confined nanocrystals in the same set of npAAO and npSi. (**D**) The UV-emitting $MAPbCl_3$ bulk compared with confined crystals in two of the smallest npSi matrices. Even this already wide-bandgap material can be blue-shifted via spatial confinement to emit below 400 nm. (**E**) Time evolution of the PL intensity during illumination at 405 nm under ambient conditions for ncMAPbBr$_3$ in npAAO (cyan empty circles) compared to bulk planar films of $MAPbBr_3$ on glass (green empty squares), evidencing encapsulation-like effects of the npAAO thin film. Sealing ncMAPbBr$_3$ samples with epoxy and glass slides (dark blue empty triangles) results in an essentially constant PL signal, demonstrating stability under continuous illumination without light-induced degradation. (**F**) PL signal for ncMAPbBr$_3$ in npAAO after 1-min (dark green), 30-min (green), and 1-day (light green) illumination at 405 nm. (**G**) Time evolution of the PL intensity during illumination at 405 nm under ambient conditions for ncCsPbBr$_3$ in npAAO (blue empty circles) and bulk $CsPbBr_3$ on glass (cyan empty squares). Epoxy- and glass-encapsulated ncCsPbBr$_3$ samples (dark blue empty triangles) again show stable PL and no photodegradation. (**H**) PL signal for ncCsPbBr$_3$ in npAAO after 1-min (light blue), 30-min (blue), and 1-day (dark blue) illumination at 405 nm.

of our nanocrystals under photoexcitation, without signs for light-induced degradation.

Size analysis

To investigate whether the observed hypsochromic shifts are size-induced, we perform structural studies. Electron microscopy is used to test for the porosity and nucleation profile, as well as to get a first indication about particle sizes. We prepare focused ion beam (FIB)–milled lamellae of npAAO and find columnar structures on large areas using BF-STEM (fig. S5). From the uniform distribution of nanopores (top-view SEM; fig. S5), we estimate a template porosity of 15%. Energy-dispersive x-ray spectroscopy (EDX) scans confirm infiltration of the npAAO with perovskite nanocrystals (fig. S5). The EDX analysis also confirms that the bright regions (due to z-contrast) imaged on exfoliated npSi/ncMAPbI$_3$ flakes in high-angle annular dark field (HAADF) (Fig. 3A) are perovskites. EDX line scans (Pb L line) from the thinnest parts of the flakes allow us to infer a size of ~4 nm for the perovskite crystals (Fig. 3B). To quantify the size of the perovskite crystallites that form in npSi, we use microfocus high-energy x-ray depth profiling in transmission geometry (fig. S6). Three npSi/ncMAPbI$_3$ samples (anodized at 15, 25, and 30 mA cm^{-2}) are probed to correlate the anodization current density with the resulting crystal size. The microfocus beam (FWHM, 2 to 5 μm; compare figs. S6 and S7) allows us to verify the formation of perovskite nanocrystals throughout the entire thickness of the npSi layers. The obtained diffraction patterns (figs. S6 and S7) are a superposition of the background due to the npSi and debye rings of the perovskite crystallites within the pores. The background-corrected azimuthally averaged MAPbI$_3$ scattering signal is extracted as a function of the scattering vector **q**. The maximal perovskite signal for each sample is shown in Fig. 3C [for intensity profiles at all depths, see figs. S6 (30 mA cm^{-2}) and S7 (15 and 25 mA cm^{-2})]. The observed peak positions obtained from the debye rings are indexed to a tetragonal structure with the lattice constants $a = b = 8.90(3)$ Å and $c = 12.71(5)$ Å. These lattice constants match the literature values of Stoumpos *et al.* (*47*), $a = b = 8.849(2)$ Å and $c = 12.642(2)$ Å within 0.6%. A complete peak indexing is given in fig. S6. All MAPbI$_3$ peaks show strong broadening due to finite crystal size. Using the Scherrer equation (*48*), we calculate the depth-dependent crystallite size (Fig. 3, D to F) from the FWHM of the diffraction peaks (see figs. S6 and S7 for details). The amount of perovskite material accumulating at a specific depth can be read off from the depth-dependent diffracted power, that is, the integrated intensity of the perovskite diffraction peaks. In all cases, we find a rather narrow distribution of crystallite size versus depth, allowing us to average over the whole layer thickness using the amount of MAPbI$_3$ at a specific depth as weights. We obtain average MAPbI$_3$ crystallite sizes of 1.8, 2.1, and 4.5 nm for 15–, 25–, and 30–mA cm^{-2} npSi, respectively. This is the same order of magnitude as values reported for the exciton Bohr radius in MAPbI$_3$ (2.2 and 2.8 nm) (*49*, *50*), accounting for the strongly blue-shifted emission observed in these nanocrystals. We further estimate the pore size and porosity of a 15–mA cm^{-2} npSi scaffold from additional x-ray experiments (fig. S8). A film porosity of 57% is determined from x-ray transmission measurements. Small-angle x-ray scattering (SAXS) experiments following the method of Porod (*51*) reveal an average pore diameter of 4.0 nm. Comparing this with the crystal size analysis, we find that the formed perovskite nanocrystals are smaller than the surrounding pores (1.8 nm versus 4.0 nm). This indicates that the pores act as weakly connected nanoreactors, placing an upper bound on the perovskite nanocrystal size. Because of this enhancement of confinement, nanocrystals consisting of only a few unit cells (about six in the case of 15–mA cm^{-2} npSi) can be achieved, which can result in pronounced PL blue shifts. Our structural characterization reveals that the average crystallite size decreases with decreasing pore size. This directly translates into an increase of the PL peak emission energy (Fig. 3G), together providing strong evidence that the observed PL blue shifts are due to quantum size effects.

Light-emitting diodes

Incorporating nanoscale (less than 10 nm) perovskite emitters as active layers in LEDs is currently pursued with colloidal dots and platelets, promising low-cost high–color purity photonic sources (*9*–*11*, *52*–*55*). The possibility and ease of 3D structuring incorporated in thin-film device architectures are unique benefits of our nanoporous solid templates. Translating this concept of solid-state confinement into devices requires electrical addressability of the nanotemplates. We demonstrate that insulating npAAO filled with perovskite aids the formation of conductive nanostructures, enabling low-voltage electroluminescent diodes (Fig. 4A) with narrow and blue-shifted emission. To fabricate nanoporous perovskite nanocrystal LEDs (npPeLEDs), a bilayer of Ti and Al is deposited onto transparent fluorine-doped tin oxide (FTO). Aluminum is anodized by electrochemical oxidation to obtain npAAO (60-nm film; Fig. 4B and fig. S9) and then infused with precursor solution to yield perovskite nanocrystals. We observe uniform PL over large areas after the npAAO is filled with perovskites from the solution (Fig. 4C), indicating the suitability of the titania/npAAO/perovskite composite films for diodes. Titanium is not porosified by the electrolyte during anodization, forming compact TiO_2 that acts as the electron injection layer in the sandwich structure. The device is completed by a hole-conducting polymer (HTL) top layer and MoOx/Ag contacts (Fig. 4A). Devices prepared with ncMAPbI$_3$ give red electroluminescence (EL) peaking at 731 nm (Fig. 4D), that is, ~60 nm blue-shifted from the NIR emitting bulk. For CsPbBr$_3$ devices, we find a sharp green-cyan EL centered at 518 nm. Its FWHM of 17 nm (Fig. 4E) is in line with the results of Li *et al.* (*53*) shown for CsPbBr$_3$ nanocrystal devices. The diodes turn on at ~2.5 V and give about 300 cd m^{-2} operating at 5 V (Fig. 4F). At this voltage, the *J*-*V* (current density–voltage) characteristics show that npAAO/perovskite layers carry a current density of about 420 mA cm^{-2}. Our perovskite LEDs have a current efficiency of ~0.09 cd A^{-1} and an external quantum efficiency of ~0.03%; however, the demonstrated PLQY of up to 90% for our perovskite nanocrystals emitters suggests that higher efficiencies are achievable through further device optimization. This is expected to match the performance of current state-of-the-art 2D- and 3D-based perovskite LEDs (*10*, *13*, *43*, *52*, *53*, *55*) while preserving the ease of color tuning. Control samples prepared without perovskite were electrically insulating. The optoelectronic quality of the composite nanoporous layer is exemplified by uniform EL over continuous areas as large as 15 mm^2 (Fig. 4G).

DISCUSSION

We demonstrated blue emission from ncCsPbBr$_3$ in npSi and cyan EL in npAAO-based LEDs. Strong blue shifts were observed for the silicon-based templates because their small pore sizes allow for crystallite sizes as small as 2 nm. Future electrical addressing of these templates seems feasible through down-scaling of the npSi matrix to sub–100-nm thicknesses via advanced silicon patterning or porosification protocols. Reducing the pore size in npAAO is expected to result in more pronounced blue shifts; feasible routes for this are optimization

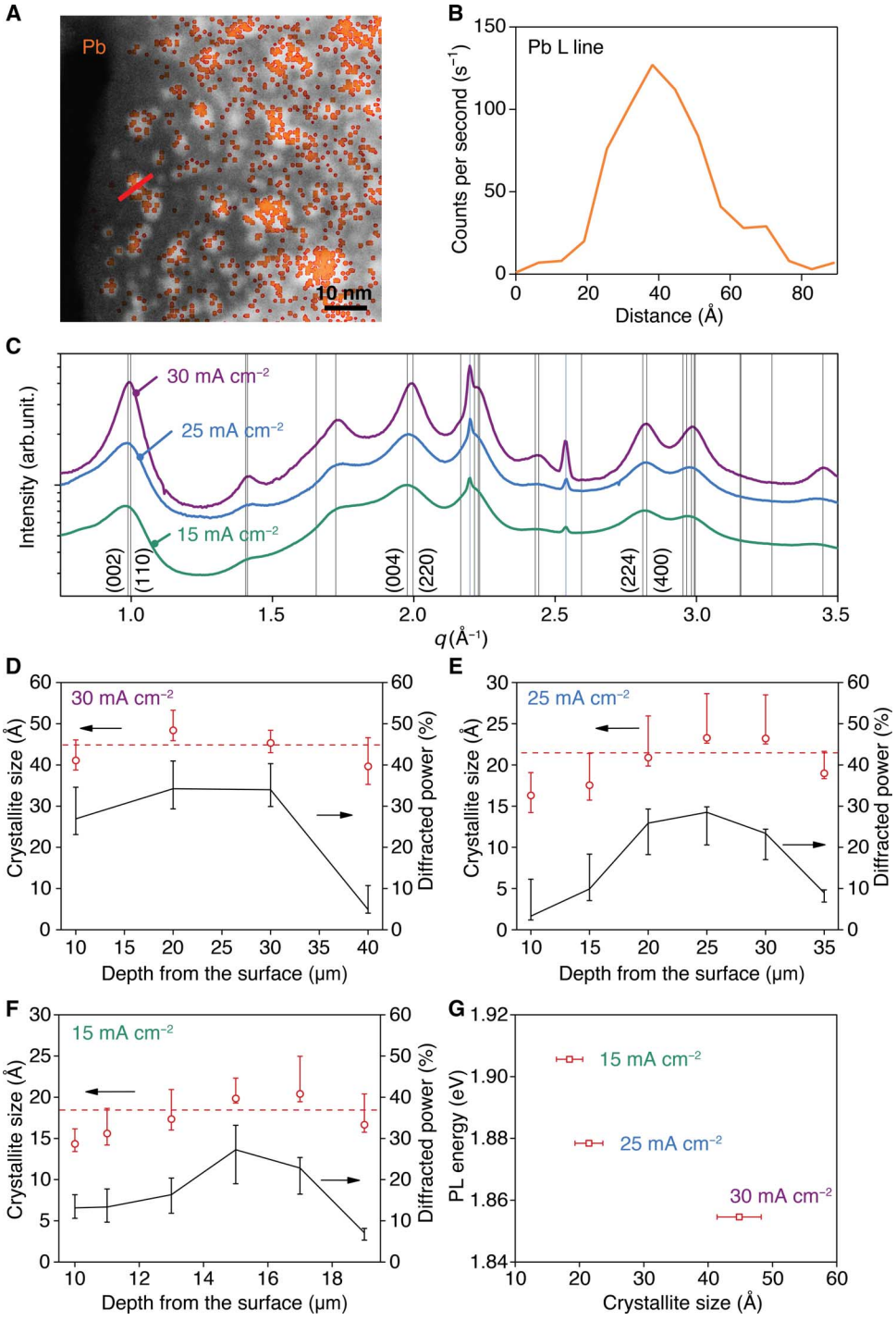

Fig. 3. Depth-resolved structural characterization of perovskite nanocrystals in npSi films. (**A**) HAADF-STEM image of an exfoliated npSi/ncMAPbI$_3$ flake. The bright regions correspond to perovskite (due to z-contrast), as confirmed by EDX analysis. The Pb signal is plotted as orange overlay. (**B**) EDX line scan (Pb L line) of a single crystallite from the thinnest part of the flake [indicated as red line in (A)]. We find a crystallite size of 4 nm for 30–mA cm^{-2} npSi. (**C**) Background corrected, azimuthally averaged x-ray diffraction profiles of MAPbI$_3$ in 30–mA cm^{-2} npSi (violet line), in 25–mA cm^{-2} npSi (blue line), and in 15–mA cm^{-2} npSi (green line) as a function of the scattering vector **q**. The curves are normalized and vertically shifted for clarity. The log-scale highlights the increasing broadening of all MAPbI$_3$ peaks with decreasing current density due to crystallite size reduction, suggesting increasingly strong confinement. The peaks are indexed to a tetragonal structure with the lattice constants $a = b = 8.90(3)$ Å and $c = 12.71(5)$ Å. (**D** to **F**) Crystallite size and diffracted power of the MAPbI$_3$ signal as function of depth for (D) 30–mA cm^{-2} npSi/ncMAPbI$_3$, (E) 25–mA cm^{-2} npSi/ncMAPbI$_3$, and (F) 15–mA cm^{-2} npSi/ncMAPbI$_3$. Red circles: Depth-dependent crystallite size. Black line: Integrated intensity of the perovskite diffraction signal as a measure for the amount of perovskite at a specific depth. Dashed red line: Weighted average of the crystallite size. Error bars correspond to the 1-σ values of the uncertainty resulting from data analysis and the initial resolution of the experiment. (**G**) PL peak emission energy against the average size of crystallites formed in three npSi layers prepared with indicated anodization current density. Error bars correspond to the SD of the crystallite size.

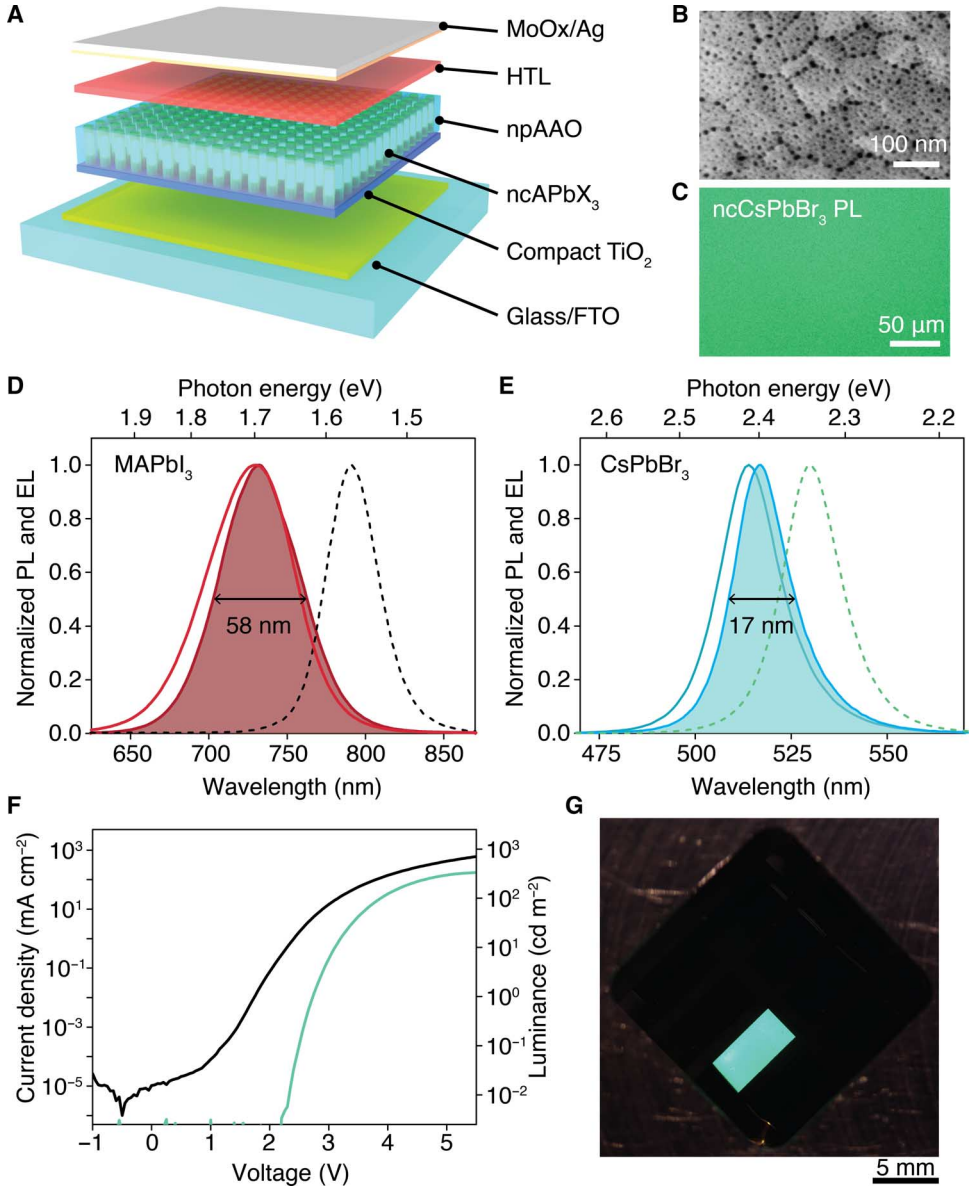

Fig. 4. Perovskite-infused nanoporous thin films for LEDs. (**A**) Schematic of npPeLEDs. Devices are fabricated on glass/FTO by anodizing a titanium/aluminum bilayer. This electrochemical procedure produces npAAO with compact TiO_2 below. Precursor solution infused to the top of the pores yields conducting and electroluminescent nanocrystalline perovskite domains. A polymeric HTL and hole-injecting contact of MoOx/Ag complete the device stack. (**B**) SEM of anodized Ti/Al, showing the npAAO layer with pores of ~6-nm diameter on top of the scale-like Ti/TiO_2 domains below. (**C**) PL micrograph image taken of a Ti/npAAO layer infused with $CsPbBr_3$, evidencing uniform light emission across large areas of the sample. Excitation filter, 465 to 495 nm; barrier filter, 515 to 555 nm. (**D**) EL of an ncMAPbI$_3$ diode, (filled curve) centered around 731 nm, with bulk PL emission (dashed line) and PL of the ncMAPbI$_3$ diode (solid curve) plotted for comparison. (**E**) EL (filled curve) of an ncCsPbBr$_3$ diode with PL emission of the bulk (dashed line) and the ncCsPbBr$_3$ diode is shown (solid line). Cyan-green narrowband EL peaking at 518 nm is observed. (**F**) *J-V* characteristic of an ncCsPbBr$_3$ diode (black trace) plotted together with luminance (cyan). Devices turn on at ~2.5 V with a luminance of ~330 cd m^{-2} at 5 V. (**G**) Photograph of a CsPbBr$_3$ diode while operating at 4 V, displaying cyan-green EL over the entire area of the pixel (15 mm^2).

of the anodization protocol or narrowing the pore diameter by deposition of conformal interlayers, for example, via atomic layer deposition. The electrical performance of our npPeLEDs is expected to further improve by reducing nonradiative recombination within the semiconductor and at the TiO_2/perovskite and perovskite/HTL interfaces or by reducing exciton quenching inside the emitting layer. The npPeLEDs presented here already reached indoor-display brightness levels, demonstrating the potential of solid-state confinement for perovskite photonic sources. Color tuning in single-halide perovskites through quantum size effects may alleviate stability issues (*56*). Forming ligand-capped 2D or 3D nanocrystals directly within our nanoporous solids may open additional routes toward size and shape control in integrated, device-compatible thin-film structures. Future work should focus on fundamental research, exploring complex lateral and depth-resolved nanostructuring for manipulation of optoelectronic properties. Potential applications range from photon detectors and (polarized) electroluminescent devices to single-photon sources and metasurfaces.

MATERIALS AND METHODS

Perovskite precursor solutions

All chemicals and solvents were purchased from commercial suppliers and used as received, if not stated otherwise. Methylammonium bromide ($MABr_3$) was synthesized from methylamine [33 weight % (wt %) in absolute ethanol; Sigma-Aldrich] and hydrobromic acid (48 wt %, aqueous; Sigma-Aldrich) and purified using diethylether (VWR) and absolute ethanol (Merck Millipore) as described in literature (*57*, *58*). Methylammonium chloride ($MACl_3$) was prepared via an analogous protocol using hydrochloric acid (37 wt %, aqueous; Merck Millipore). Lead bromide ($PbBr_2$; 99.999%), dimethyl sulfoxide (DMSO; ≥99%), and methylammonium iodide (MAI) were supplied by Sigma-Aldrich, Merck Millipore, and Dyesol, respectively. Lead iodide (PbI_2; 99.9985%), cesium bromide (CsBr; 99.999%), and dimethyl formamide (DMF; 99.8%) were purchased from Alfa Aesar. All parent solutions were passed through polytetrafluoroethylene syringe filters (0.45 μm; Whatman). For $MAPbI_3$, PbI_2 (922 mg, 2.00 mmol), MAI (334 mg, 2.10 mmol), and DMF (2.25 ml) were mixed to yield a clear yellow solution. For $MAPbBr_3$, $PbBr_2$ (368 mg, 1.00 mmol), MABr (124 mg, 1.11 mmol), and DMF (1.10 ml) were heated to 50°C overnight to yield a clear colorless solution. For $MAPbCl_3$, $PbCl_2$ (280 mg, 1.01 mmol), MACl (76 mg, 1.13 mmol), and DMSO (500 μl) were heated to 60°C to yield a clear colorless solution. For $CsPbBr_3$, stirring a mixture of $PbBr_2$ (367 mg, 1.00 mmol), CsBr (215 mg, 1.01 mmol), and DMSO (2.4 ml) overnight at 70°C resulted in a clear colorless solution. Iodide-bromide– and bromide-chloride–containing precursors were prepared from single-halide solutions by mixing at an 80:20 volume ratio.

Nanoporous silicon

Two types of boron-doped p-type silicon wafers with thickness of 0.5 mm and <100> orientation were used: either "low-doped," with R_0 = 8 to 20 ohm cm, or "highly-doped," with R_0 = 0.01 ohm cm. The wafers were polished on one side, with an alkaline-etched backside. The Si wafers were cut into 1″ × 1″ squares, cleaned by ultrasonication sequentially in 2% solution of chemical detergent Hellmanex III, deionized water, acetone, and 2-propanol, followed by the RCA (Radio Corporation of America) standard cleaning steps (*59*). Next, 250-nm aluminum contacts were evaporated onto the alkaline-etched side. After the deposition of the Al, the samples were annealed in N_2 atmosphere for 20 min at 450°C to ensure an ohmic Al/p Si contact. The polished surface of the substrate was nanostructured by anodization in the standard etch cell as defined by Sailor (*42*). Contact to the silicon substrate was established by directly contacting aluminum foil with the aluminized back of the substrate, whereas the counter electrode was a platinum coil. Anodization was conducted in the galvanostatic mode using a Keithley 2400 SourceMeter with variable current density: 5 to 30 mA cm^{-2} for low-doped Si and 150 to 370 mA cm^{-2} for highly doped Si. Anodization was performed for 20 min for all the samples. The electrolyte consisted of a mixture of 48% HF and ethanol in a volumetric ratio of 1:1 for low-doped Si and 4:1 for highly doped Si. Following anodization, the electrolyte was removed with a plastic micropipette, and the sample was thoroughly washed with ethanol and dried under a N_2 stream. Next, the npSi samples were treated with oxygen plasma (Plasma Etch PE-25-JW) for 5 min at 50 W, resulting in a highly hydrophilic surface that is readily wetted by the DMF and DMSO perovskite precursor solutions. The solutions were deposited by spin-coating at 2400 rpm for 7 s and afterward annealed for 30 min at 115°C in ambient atmosphere.

Anodic aluminum oxide nanotubes (npAAO)

Glass substrates (1″ × 1″) 1 mm thick were cleaned by ultrasonication sequentially in Hellmanex III chemical detergent solution (2 volume %, aqueous), deionized water, acetone, and 2-propanol, followed by oxygen plasma cleaning for 5 min at 50 W. Varying thicknesses (20 nm to 1 μm) of aluminum were thermally evaporated onto the glass slides at a rate of 1 to 5 nm s^{-1} and a base pressure of ~1 × 10^{-6} mbar. The samples were then anodized potentiostatically using a Keithley 2400 SourceMeter in an aqueous 0.2 M oxalic acid solution and a platinum foil counter electrode. Small pores (<8 nm) were achieved using an anodization voltage of 5 V. The aluminum films were contacted using an alligator clip and partially immersed into the electrolyte. The region at the air-electrolyte interface was masked with polyimide tape to prevent rapid electrochemical etching at the top of the sample. Anodization was continued until the steady-state anodization current rapidly dropped, signaling that the conductive aluminum layer had been completely consumed. At this point, the npAAO film was visibly transparent and featured a blue-green iridescence. The npAAO samples were then rinsed with 18-megohm water, dried, and treated with oxygen plasma for 5 min at 50 W before infiltration with perovskite precursor solutions.

Nanoporous perovskite nanocrystal LEDs

Patterned FTO-coated glass slides (Xin Yan Technology Ltd.; 1″ × 1″ with a centered, 1.35-cm-wide and 2.5-cm-long stripe of FTO with a sheet resistance of 15 ohms per square) were polished with a titanium- and silicon oxide–containing polishing paste to improve surface qualities. The FTO-coated glass slides were further cleaned using sequential ultrasonication as described for the npAAO preparation and subsequently treated with oxygen plasma (50 W for 5 min). Layers of titanium (15 nm) and aluminum (40 nm) were evaporated sequentially on top of the FTO in the same thermal evaporation system without breaking vacuum, with deposition rates of 0.1 and 1 nm s^{-1} at a base pressure of 1 × 10^{-6} mbar. Anodization of the double layer was performed as described above. This one-pot anodization protocol resulted in an optically transparent npAAO scaffold atop a compact titania film. This functional oxide double-layer architecture served both as electron injection contact and as insulating nanoscale template for the formation of conjoined perovskite nanocrystals. After rinsing with 18-megohm water and drying, samples were treated with oxygen plasma (50 W for 5 min). The perovskite precursor solutions (parent solution of $CsPbBr_3$ diluted in a volume ratio of 1:22 with DMF or parent solution of $MAPbI_3$ diluted in a volume ratio of 1:15 with DMF) were deposited by spin-coating at 2400 rpm for 7 s. These recipes allowed filling of the 60-nm high-porous matrix without the formation of bulk perovskite layers, resulting in electrically addressable conjoined nanocrystals. The samples were annealed for 30 min at 115°C in ambient atmosphere. Poly[9,9-dioctylfluorenyl-2,7-diyl] end-capped with *N*,*N*-bis(4-methylphenyl)-aniline (F8, purchased from ADS; 0.5 wt %), dissolved in chlorobenzene, was spin-coated at 3000 rpm until dry-yielding a hole-transporting polymer layer. Molybdenum(VI) oxide (20 nm) and silver (100 nm), thermally deposited at rates of 0.03 and 1 nm s^{-1} through a metal shadow mask at a base pressure of ~1 × 10^{-6} mbar, completed the device.

High-energy x-ray diffraction

The measurements were performed at the high-energy beamline (P07) at PETRA III at DESY (Deutsches Elektronen-Synchrotron). The 30–mA cm^{-2} npSi/ncMAPbI$_3$ sample was measured with an x-ray beam with an energy of 98.5 keV, which was focused down to a spot

of 5 μm × 50 μm (vertical × horizontal FWHM) at the sample position using Al compound refractive lenses. For all other samples, the respective values were 80.0 keV and 2 μm × 30 μm. The diffracted intensity was recorded 2000 mm behind the sample by a PerkinElmer XRD 1621 flat panel detector. To distinguish clearly between the signal of the perovskite and the background resulting from the substrate, a reference npSi sample without perovskite was measured for each beam configuration. For data processing, Igor Pro (WaveMetrics), including the "Nika" package (*60*), and OriginPro (OriginLab) were used (see the Supplementary Materials for details).

Small-angle x-ray diffraction

The samples were measured in transmission with the surface perpendicular to a 20.0-keV x-ray beam at beamline P08 at PETRA III at DESY. The scattered intensity was detected by a PerkinElmer XRD 1621 flat panel detector at a distance of 2440 mm behind the sample. For data analysis, the "Nika" package (*60*) for Igor Pro (WaveMetrics) and SASfit (*61*) were used.

Scanning transmission electron microscopy

The npSi specimens were prepared by mechanical exfoliation from the porous areas of the sample on a holey carbon TEM grid. The npAAO specimens were prepared by FIB milling (1540 CrossBeam SEM, Zeiss). A thin gold layer was sputtered onto the specimen before milling. TEM lamellae were prepared by standard FIB cutting, lifting out, and transferring to a TEM grid, followed by a final thinning to about 100 nm with an ion energy of 5 keV to minimize preparation artifacts. STEM was performed in BF and HAADF modes, sensitive to the z-contrast of the Pb-rich regions. Line and mapping analyses where carried out using EDX. All specimens were investigated with a JEOL JEM-2200FS TEM under STEM mode operated at 200 kV, and an Oxford SDD X-MaxN (80 mm^2) EDX system.

Sample characterization

Surface SEM measurements were made using the Zeiss 1540 XB CrossBeam SEM. Optical microscopy images were recorded using a Nikon Eclipse LV100ND microscope with up to ×400 magnification and a PL filter cube accessory. PL spectra were recorded on a photomultiplier tube–equipped double-grating input and output fluorometer (Photon Technology International). EL measurements were performed using a Shamrock SR-303i monochromator, an Andor iDus Si-CCD camera, and a Keithley 2400 SourceMeter. The optical power output of the npPeLEDs was measured with an Agilent B1500 parameter analyzer and a calibrated silicon diode (S2281, Hamamatsu).

PL quantum efficiency

Samples were prepared as described before, using a 150-nm-thick layer of npAAO on glass. Bulk references were also prepared on glass. Several samples were prepared for each of the systems with varying concentrations of precursor solutions ranging from 0.06 to 0.1 M. The PL quantum efficiency was measured using a method previously described in literature (*62*). The measurement was performed inside an integrating sphere in a fluorometer (Photon Technology International), and the excitation wavelength was 405 nm with an illumination intensity of approximately 0.4 mW cm^{-2}.

PL stability measurements

Samples were prepared with 150 nm of npAAO on glass and 0.08 M solution of $CsPbBr_3$ or $MAPbBr_3$. Samples were placed in a fluorometer (Photon Technology International), and the spectra were recorded for about 28 hours. Peak intensity was used for the data evaluation. Peak wavelength was monitored, and it showed no variation throughout the duration of the measurement. Encapsulated samples of perovskite nanocrystals in npAAO were sealed with UV curable epoxy (Ozilla E131) and glass slides.

Time-resolved PL lifetime measurements

Bulk $MAPbI_3$, $MAPbBr_3$, and $CsPbBr_3$ films were measured using an yttrium-aluminum-garnet–Nd laser (Spitlight Compact 100) emitting at 355 or 532 nm with a pulse length of ~10 ns and an energy of 50 μJ cm^{-2} in both cases. The spot size was 5 mm in diameter. Signal detection was performed with a Shamrock spectrometer (SR-303i-A), equipped with an intensified charge-coupled device camera [Andor iStar DH320T-18U-73 (gate step, 2.5 ns; gate width, 2.5 ns)]. The samples were kept under vacuum during the measurement. Corresponding shorter-lived perovskite nanocrystals in 5–mA cm^{-2} npSi templates were investigated using a superconducting single photon detector (SSPD; Scontel Superconducting Nanotechnology) together with a time-correlated single-photon counting system (PicoHarp 300 by PicoQuant). The time resolution of the SSPD system is about 300 ps. Samples were excited by a pulsed diode laser (405 nm) delivering ~1-ns pulses (FWHM) at repetition rates of 1 MHz and pulse energies of approximately 5 pJ. A microscope objective was used to focus the laser onto a spot with a 10-μm diameter on the sample surface. The sample emission was collected using the same microscope objective, and the photons were guided through a single-mode fiber to the SSPD. A long-pass filter was applied to block the excitation before entering the fiber connected to the SSPD.

SUPPLEMENTARY MATERIALS

Supplementary material for this article is available at http://advances.sciencemag.org/cgi/content/full/3/8/e1700738/DC1

fig. S1. Bandgap tuning via size effects and halide compositional stoichiometry in npSi and npAAO.
fig. S2. PL of native npSi and $MAPbI_3$ nanocrystals in npSi.
fig. S3. Fine-tuning of the bandgap in npSi via variation of pore size.
fig. S4. Time-resolved PL lifetime.
fig. S5. Structural characterization of $MAPbBr_3$ nanocrystals in npAAO.
fig. S6. Wide-angle x-ray scattering (WAXS) study of $MAPbI_3$ nanocrystals in 30–mA cm^{-2} npSi: Experiment and data analysis.
fig. S7. WAXS study of $MAPbI_3$ nanocrystals in 15–mA cm^{-2} npSi and 25–mA cm^{-2} npSi.
fig. S8. Pore size estimation by Porod analysis of SAXS data of 15–mA cm^{-2} npSi.
fig. S9. Surface SEM of npAAO on compact TiO_2.
References (*63*–*67*)

REFERENCES AND NOTES

1. D. Zhao, M. Sexton, H.-Y. Park, G. Baure, J. C. Nino, F. So, High-efficiency solution-processed planar perovskite solar cells with a polymer hole transport layer. *Adv. Energy Mater.* **5**, 1–5 (2015).
2. M. Yuan, M. Liu, E. H. Sargent, Colloidal quantum dot solids for solution-processed solar cells. *Nat. Energy* **1**, 16016 (2016).
3. P. O. Anikeeva, J. E. Halpert, M. G. Bawendi, V. Bulović, Quantum dot light-emitting devices with electroluminescence tunable over the entire visible spectrum. *Nano Lett.* **9**, 2532–2536 (2009).
4. S. Chen, W. Li, J. Wu, Q. Jiang, M. Tang, S. Shutts, S. N. Elliott, A. Sobiesierski, A. J. Seeds, I. Ross, P. M. Smowton, H. Liu, Electrically pumped continuous-wave III–V quantum dot lasers on silicon. *Nat. Photonics* **10**, 307–311 (2016).
5. B. Saparov, D. B. Mitzi, Organic–inorganic perovskites: Structural versatility for functional materials design. *Chem. Rev.* **116**, 4558–4596 (2016).
6. A. H. L. Kazmerski, D. Gwinner, Best research cell efficiencies. *Natl. Renew. Energy Lab.* (2010); www.nrel.gov/pv/assets/images/efficiency-chart.png.
7. M. Kaltenbrunner, G. Adam, E. D. Głowacki, M. Drack, R. Schwödiauer, L. Leonat, D. H. Apaydin, H. Groiss, M. C. Scharber, M. S. White, N. S. Sariciftci, S. Bauer, Flexible high power-per-weight perovskite solar cells with chromium oxide–metal contacts for improved stability in air. *Nat. Mater.* **14**, 1032–1039 (2015).

8. S. D. Stranks, H. J. Snaith, Metal-halide perovskites for photovoltaic and light-emitting devices. *Nat. Nanotechnol.* **10**, 391–402 (2015).
9. S. A. Veldhuis, P. P. Boix, N. Yantara, M. Li, T. C. Sum, N. Mathews, S. G. Mhaisalkar, Perovskite materials for light-emitting diodes and lasers. *Adv. Mater.* **28**, 6804–6834 (2016).
10. Y.-H. Kim, H. Cho, T.-W. Lee, Metal halide perovskite light emitters. *Proc. Natl. Acad. Sci. U.S.A.* **113**, 11694–11702 (2016).
11. B. R. Sutherland, E. H. Sargent, Perovskite photonic sources. *Nat. Photonics* **10**, 295–302 (2016).
12. Y.-H. Kim, H. Cho, J. H. Heo, T.-S. Kim, N. Myoung, C.-L. Lee, S. H. Im, T.-W. Lee, Multicolored organic/inorganic hybrid perovskite light-emitting diodes. *Adv. Mater.* **27**, 1248–1254 (2015).
13. H.-K. Seo, H. Kim, J. Lee, M.-H. Park, S.-H. Jeong, Y.-H. Kim, S.-J. Kwon, T.-H. Han, S. Yoo, T.-W. Lee, Efficient flexible organic/inorganic hybrid perovskite light-emitting diodes based on graphene anode. *Adv. Mater.* **29**, 1605587 (2017).
14. G. Nedelcu, L. Protesescu, S. Yakunin, M. I. Bodnarchuk, M. J. Grotevent, M. V. Kovalenko, Fast anion-exchange in highly luminescent nanocrystals of cesium lead halide perovskites ($CsPbX_3$, X = Cl, Br, I). *Nano Lett.* **15**, 5635–5640 (2015).
15. L. Protesescu, S. Yakunin, M. I. Bodnarchuk, F. Krieg, R. Caputo, C. H. Hendon, R. X. Yang, A. Walsh, M. V. Kovalenko, Nanocrystals of cesium lead halide perovskites ($CsPbX_3$, X = Cl, Br, and I): Novel optoelectronic materials showing bright emission with wide color gamut. *Nano Lett.* **15**, 3692–3696 (2015).
16. D. B. Mitzi, Organic-inorganic perovskites and related materials, in *Progress in Inorganic Chemistry*, K. D. Karlin, Ed. (John Wiley & Sons, 1999), pp. 1–121.
17. C. R. Kagan, C. R. Kagan, D. B. Mitzi, C. D. Dimitrakopoulos, Organic-inorganic hybrid materials as semiconducting channels in thin-film field-effect transistors. *Science* **286**, 945–947 (1999).
18. L. C. Schmidt, A. Pertegaś, S. Gonzaĺez-Carrero, O. Malinkiewicz, S. Agouram, G. M. Espallargas, H. J. Bolink, R. E. Galian, J. Peŕez-Prieto, Nontemplate synthesis of $CH_3NH_3PbBr_3$ perovskite nanoparticles. *J. Am. Chem. Soc.* **136**, 850–853 (2014).
19. J. A. Sichert, Y. Tong, N. Mutz, M. Vollmer, K. Z. Milowska, R. G. Cortadella, B. Nickel, C. Cardenas-Daw, J. K. Stolarczyk, A. S. Urban, J. Feldmann, Quantum size effect in organometal halide perovskite nanoplatelets. *Nano Lett.* **15**, 6521–6527 (2015).
20. Y. Hassan, Y. Song, R. D. Pensack, A. I. Abdelrahman, Y. Kobayashi, M. A. Winnik, G. D. Scholes, Structure-tuned lead halide perovskite nanocrystals. *Adv. Mater.* **28**, 566–573 (2016).
21. H. Huang, F. Zhao, L. Liu, F. Zhang, X. G. Wu, L. Shi, Q. Peng, H. Zhong, Emulsion synthesis of size-tunable $CH_3NH_3PbBr_3$ quantum dots: An alternative route toward efficient light-emitting diodes. *ACS Appl. Mater. Interfaces* **7**, 28128–28133 (2015).
22. Y. Niu, F. Zhang, Z. Bai, Y. Dong, J. Yang, R. Liu, B. Zou, J. Li, H. Zhong, Aggregation-induced emission features of organometal halide perovskites and their fluorescence probe applications. *Adv. Opt. Mater.* **3**, 112–119 (2015).
23. F. Zhu, L. Men, Y. Guo, Q. Zhu, U. Bhattacharjee, P. M. Goodwin, J. W. Petrich, E. A. Smith, J. Vela, Shape evolution and single particle luminescence of organometal halide perovskite nanocrystals. *ACS Nano* **9**, 2948–2959 (2015).
24. H. Huang, A. S. Susha, S. V. Kershaw, T. F. Hung, A. L. Rogach, Control of emission color of high quantum yield $CH_3NH_3PbBr_3$ perovskite quantum dots by precipitation temperature. *Adv. Sci.* **2**, 1500194 (2015).
25. P. Tyagi, S. M. Arveson, W. A. Tisdale, Colloidal organohalide perovskite nanoplatelets exhibiting quantum confinement. *J. Phys. Chem. Lett.* **6**, 1911–1916 (2015).
26. S. Aharon, L. Etgar, Two dimensional organometal halide perovskite nanorods with tunable optical properties. *Nano Lett.* **16**, 3230–3235 (2016).
27. V. Malgras, S. Tominaka, J. W. Ryan, J. Henzie, K. Ohara, Y. Yamauchi, Observation of quantum confinement in monodisperse methylammonium lead halide perovskite nanocrystals embedded in mesoporous silica. *J. Am. Chem. Soc.* **138**, 13874–13881 (2016).
28. D. N. Dirin, L. Protesescu, D. Trummer, I. V. Kochetygov, S. Yakunin, F. Krumeich, N. P. Stadie, M. V. Kovalenko, Harnessing defect-tolerance at the nanoscale: Highly luminescent lead halide perovskite nanocrystals in mesoporous silica matrixes. *Nano Lett.* **16**, 5866–5874 (2016).
29. A. Kojima, M. Ikegami, K. Teshima, T. Miyasaka, Highly luminescent lead bromide perovskite nanoparticles synthesized with porous alumina media. *Chem. Lett.* **41**, 397–399 (2012).
30. G. Longo, A. Pertegás, L. Martínez-Sarti, M. Sessolo, H. J. Bolink, Highly luminescent perovskite-aluminum oxide composites. *J. Mater. Chem. C* **3**, 11286–11289 (2015).
31. M. I. J. Beale, J. D. Benjamin, M. J. Uren, N. G. Chew, A. G. Cullis, An experimental and theoretical study of the formation and microstructure of porous silicon. *J. Cryst. Growth* **73**, 622–636 (1985).
32. R. Herino, G. Bomchil, K. Barla, C. Bertrand, J. L. Ginoux, Porosity and pore size distributions of porous silicon layers. *J. Electrochem. Soc.* **134**, 1994–2000 (1987).
33. L. T. Canham, Laser dye impregnation of oxidized porous silicon on silicon wafers. *Appl. Phys. Lett.* **63**, 337–339 (1993).
34. E. D. Glowacki, M. Irimia-Vladu, M. Kaltenbrunner, J. Gsiorowski, M. S. White, U. Monkowius, G. Romanazzi, G. P. Suranna, P. Mastrorilli, T. Sekitani, S. Bauer, T. Someya, L. Torsi, N. S. Sariciftci, Hydrogen-bonded semiconducting pigments for air-stable field-effect transistors. *Adv. Mater.* **25**, 1563–1569 (2013).
35. D. Qi, K. Kwong, K. Rademacher, M. O. Wolf, J. F. Young, Optical emission of conjugated polymers adsorbed to nanoporous alumina. *Nano Lett.* **3**, 1265–1268 (2003).
36. T. P. Nguyen, S. H. Yang, P. Le Rendu, H. Khan, Optical properties of poly(2-methoxy-5-(2'-ethyl-hexyloxy)-phenylene vinylene) deposited on porous alumina substrates. *Compos. Part A Appl. Sci. Manuf.* **36**, 515–519 (2005).
37. M. Lai, D. J. Riley, Templated electrosynthesis of nanomaterials and porous structures. *J. Colloid Interface Sci.* **323**, 203–212 (2008).
38. G. Korotcenkov, B. K. Cho, Silicon porosification: State of the art. *Crit. Rev. Solid State Mater. Sci.* **35**, 153–260 (2010).
39. P. Granitzer, K. Rumpf, Porous silicon—A versatile host material. *Materials* **3**, 943–998 (2010).
40. A. Miyata, A. Mitioglu, P. Plochocka, O. Portugall, J. T.-W. Wang, S. D. Stranks, H. J. Snaith, R. J. Nicholas, Direct measurement of the exciton binding energy and effective masses for charge carriers in organic–inorganic tri-halide perovskites. *Nat. Phys.* **11**, 582–587 (2015).
41. K. Galkowski, A. Mitioglu, A. Miyata, P. Plochocka, O. Portugall, G. E. Eperon, J. T.-W. Wang, T. Stergiopoulos, S. D. Stranks, H. J. Snaith, R. J. Nicholas, Determination of the exciton binding energy and effective masses for the methylammonium and formamidinium lead tri-halide perovskite family. *Energy Environ. Sci.* **9**, 962–970 (2015).
42. M. J. Sailor, *Porous Silicon in Practice* (Wiley-VCH Verlag GmbH & Co. KGaA, 2012).
43. J. Byun, H. Cho, C. Wolf, M. Jang, A. Sadhanala, R. H. Friend, H. Yang, T.-W. Lee, Efficient visible quasi-2D perovskite light-emitting diodes. *Adv. Mater.* **28**, 7515–7520 (2016).
44. A. F. van Driel, G. Allan, C. Delerue, P. Lodahl, W. L. Vos, D. Vanmaekelbergh, Frequency-dependent spontaneous emission rate from CdSe and CdTe nanocrystals: Influence of dark states. *Phys. Rev. Lett.* **95**, 236804 (2005).
45. V. D'Innocenzo, A. R. S. Kandada, M. De Bastiani, M. Gandini, A. Petrozza, Tuning the light emission properties by band gap engineering in hybrid lead-halide perovskite. *J. Am. Chem. Soc.* **136**, 17730–17733 (2014).
46. Y. Tian, M. Peter, E. Unger, M. Abdellah, K. Zheng, T. Pullerits, A. Yartsev, V. Sundström, I. G. Scheblykina, Mechanistic insights into perovskite photoluminescence enhancement: Light curing with oxygen can boost yield thousandfold. *Phys. Chem. Chem. Phys.* **17**, 24978–24987 (2015).
47. C. C. Stoumpos, C. D. Malliakas, M. G. Kanatzidis, Semiconducting tin and lead iodide perovskites with organic cations: Phase transitions, high mobilities, and near-infrared photoluminescent properties. *Inorg. Chem.* **52**, 9019–9038 (2013).
48. P. Scherrer, Bestimmung der Größe und der inneren Struktur von Kolloidteilchen mittels Röntgenstrahlen. *Göttinger Nachrichten Gesell.* **2**, 98–100 (1918).
49. K. Tanaka, T. Takahashi, T. Ban, T. Kondo, K. Uchida, N. Miura, Comparative study on the excitons in lead-halide-based perovskite-type crystals $CH_3NH_3PbBr_3$ $CH_3NH_3PbI_3$. *Solid State Commun.* **127**, 619–623 (2003).
50. M. Hirasawa, T. Ishihara, T. Goto, K. Uchida, N. Miura, Magnetoabsorption of the lowest exciton in perovskite-type compound $(CH_3NH_3)PbI_3$. *Phys. B Condens. Matter* **201**, 427–430 (1994).
51. G. Porod, *Small Angle X-ray Scattering* (Academic Press, 1982).
52. X. Zhang, H. Lin, H. Huang, C. Reckmeier, Y. Zhang, W. C. Choy, A. L. Rogach, Enhancing the brightness of cesium lead halide perovskite nanocrystal based green light-emitting devices through the interface engineering with perfluorinated ionomer. *Nano Lett.* **16**, 1415–1420 (2016).
53. G. Li, F. W. Rivarola, N. J. Davis, S. Bai, T. C. Jellicoe, F. de la Peña, S. Hou, C. Ducati, F. Gao, R. H. Friend, N. C. Greenham, Z. K. Tan, Highly efficient perovskite nanocrystal light-emitting diodes enabled by a universal crosslinking method. *Adv. Mater.* **28**, 3528–3534 (2016).
54. H. Cho, S.-H. Jeong, M.-H. Park, Y.-H. Kim, C. Wolf, C.-L. Lee, J. H. Heo, A. Sadhanala, N. S. Myoung, S. Yoo, S. H. Im, R. H. Friend, T.-W. Lee, Overcoming the electroluminescence efficiency limitations of perovskite light-emitting diodes. *Science* **350**, 1222–1225 (2015).
55. S. Kumar, J. Jagielski, S. Yakunin, P. Rice, Y.-C. Chiu, M. Wang, G. Nedelcu, Y. Kim, S. Lin, E. J. G. Santos, M. V. Kovalenko, C.-J. Shih, Efficient blue electroluminescence using quantum-confined two-dimensional perovskites. *ACS Nano* **10**, 9720–9729 (2016).
56. J. Wang, N. Wang, Y. Jin, J. Si, Z.-K. Tan, H. Du, L. Cheng, X. Dai, S. Bai, H. He, Z. Ye, M. L. Lai, R. H. Friend, W. Huang, Interfacial control toward efficient and low-voltage perovskite light-emitting diodes. *Adv. Mater.* **27**, 2311–2316 (2015).
57. N. J. Jeon, J. H. Noh, Y. C. Kim, W. S. Yang, S. Ryu, S. I. Seok, Solvent engineering for high-performance inorganic–organic hybrid perovskite solar cells. *Nat. Mater.* **13**, 897–903 (2014).
58. W. S. Yang, J. H. Noh, N. J. Jeon, Y. C. Kim, S. Ryu, J. Seo, S. I. Seok, High-performance photovoltaic perovskite layers fabricated through intramolecular exchange. *Science* **348**, 1234–1237 (2015).

59. W. Kern, D. A. Puotinen, Cleaning solution based on hydrogen peroxide for use in silicon semiconductor technology. *RCA Rev.* **31**, 187–206 (1970).
60. J. Ilavsky, *Nika*: Software for two-dimensional data reduction. *J. Appl. Crystallogr.* **45**, 324–328 (2012).
61. I. Breßler, J. Kohlbrecher, A. F. Thünemann, *SASfit*: A tool for small-angle scattering data analysis using a library of analytical expressions. *J. Appl. Crystallogr.* **48**, 1587–1598 (2015).
62. J. C. de Mello, H. F. Wittmannn, R. H. Friend, An improved experimental determination of external photoluminescence quantum efficiency. *Adv. Mater.* **9**, 230–232 (1997).
63. L. Canham, *Properties of Porous Silicon* (Institution of Electrical Engineers, 1997).
64. L. Canham, *Handbook of Porous Silicon* (Springer, 2014).
65. K. Lejaeghere, V. Van Speybroeck, G. Van Oost, S. Cottenier, Error estimates for solid-state density-functional theory predictions: An overview by means of the ground-state elemental crystals. *Crit. Rev. Solid State Mater. Sci.* **39**, 1–24 (2014).
66. R. Wyckoff, *Crystal Structures* (Interscience Publishers, 1963).
67. P. Laggner, M. Strobl, P. Jocham, P. Abuja, M. Kriechbaum, *In-situ SAXS on Transformations of Mesoporous and Nanostructured Solids* (Elsevier Science and Technology, 2007).

Acknowledgments: We thank Florian Hackl for technical assistance with PL measurements. **Funding:** This work was supported by the European Research Council Advanced Investigators Grant "Soft-Map" for S.B. and the FWF Wittgenstein Award (Solare Energie Umwandlung Z222-N19) for N.S.S. H.G. acknowledges funding from the Austrian Federal Ministry of Science, Research and Economy and the National Foundation for Research, Technology and Development. J.M.R. and B.N. acknowledge funding by the Bavarian State Ministry of Science, Research, and Arts through the grant "Solar Technologies Go Hybrid (SolTech)" and by the DFG through SFB 1032. E.D.G. acknowledges support from the Knut and Alice Wallenberg Foundation within the framework of the Wallenberg Centre for Molecular Medicine at Linköping University. Parts of this research were carried out at the light source PETRA III at DESY (Deutsches Elektronen-Synchrotron), a member of the Helmholtz Association (HGF), using beamline P07 and P08. **Author contributions:** E.D.G. and M.K. conceived and supervised the research. S.D., E.D.G., and M.K. fabricated and characterized the samples and devices. C.U. prepared the perovskite solutions. S.D., H.H., and M.C.S. measured the EL and PL. J.M.R., A.B., U.R., F.B., and B.N. performed the x-ray experiments, and J.M.R., A.B., and B.N. analyzed the data. H.G. and G.H. performed the STEM/EDX measurements and analyzed the data. D.A. obtained the SEM images. S.D., J.M.R., S.B., E.D.G., and M.K. analyzed the data, designed the figures, and wrote the manuscript with comments from all co-authors. N.S.S., S.B., E.D.G., and M.K. coordinated the project. **Competing interests:** The authors declare that they have no competing interests. **Data and materials availability:** All data needed to evaluate the conclusions in the paper are present in the paper and/or the Supplementary Materials. Additional data related to this paper may be requested from the authors.

Submitted 10 March 2017
Accepted 27 June 2017
Published 4 August 2017
10.1126/sciadv.1700738

Citation: S. Demchyshyn, J. M. Roemer, H. Groiß, H. Heilbrunner, C. Ulbricht, D. Apaydin, A. Böhm, U. Rütt, F. Bertram, G. Hesser, M. C. Scharber, N. S. Sariciftci, B. Nickel, S. Bauer, E. D. Głowacki, M. Kaltenbrunner, Confining metal-halide perovskites in nanoporous thin films. *Sci. Adv.* **3**, e1700738 (2017).

Confining metal-halide perovskites in nanoporous thin films

Stepan Demchyshyn, Janina Melanie Roemer, Heiko Groiß, Herwig Heilbrunner, Christoph Ulbricht, Dogukan Apaydin, Anton Böhm, Uta Rütt, Florian Bertram, Günter Hesser, Markus Clark Scharber, Niyazi Serdar Sariciftci, Bert Nickel, Siegfried Bauer, Eric Daniel Glowacki and Martin Kaltenbrunner

Sci Adv **3** (8), e1700738.
DOI: 10.1126/sciadv.1700738